JOURNAL OF GEOPHYSICAL RESEARCH, VOL. 113, C08033, doi:10.1029/2007JC004585, 2008

Assimilation of high-frequency radar currents in a nested model of the West Florida Shelf

A. Barth,[1,2] A. Alvera-Azcárate,[1,2] and R. H. Weisberg[2]

Received 10 October 2007; revised 5 March 2008; accepted 21 March 2008; published 19 August 2008.

[1] High-frequency radar currents are assimilated in a West Florida Shelf (WFS) model based on the Regional Ocean Model System (ROMS), which is nested in the Atlantic Hybrid Coordinate Ocean Model (HYCOM) for the purpose of including both local and deep-ocean forcing, particularly the Gulf of Mexico Loop Current. Tides are not included in this model. An ensemble simulation of the WFS model is carried out under different wind-forcings in order to estimate the error covariance of the model state vector and the covariance between ocean currents and winds. Radial currents measured by high-frequency radar antennas near Saint Petersburg and Venice, Florida, USA, are assimilated using this ensemble-based error covariance. Different assimilation techniques using a time-average ensemble, a filter to reduce surface-gravity waves and an extended state vector including wind stress were tested. Results of the WFS model assimilating surface currents show an improvement of the model currents not only at the surface but also at depth.

Citation: Barth, A., A. Alvera-Azcárate, and R. H. Weisberg (2008), Assimilation of high-frequency radar currents in a nested model of the West Florida Shelf, *J. Geophys. Res.*, *113*, C08033, doi:10.1029/2007JC004585.

1. Introduction

[2] High-frequency (HF) radar is a relatively new remote sensing technique with a large potential for describing coastal ocean surface currents. Unlike deep-ocean models where surface currents can be estimated from satellite altimetry, the accuracy and temporal resolution of sea surface height measured by altimetry are too low for coastal applications [*Volkov et al.*, 2007]. HF radar measurements (see *Barrick et al.* [1977] and *Barrick* [1978] for early accounts of the technique) have the potential to fill the gap and to provide surface current estimates on the shelf with broad spatial coverage (i.e., several hundreds of km).

[3] In numerous places, the surface circulation in coastal regions is primarily driven by winds. Regional ocean models generally use numerical weather prediction wind fields whose accuracy is limited near the coast because of complex coastline geometry, coarse resolution and missing physics in the coastal regions. As a result, errors in the wind field are transferred to the model currents. In addition to errors in wind-forcing, errors in the turbulence parametrization, stratification and the pressure gradient scheme degrade coastal ocean model simulations. In this work, HF radar currents are used to constrain the evolution of a model by data assimilation.

[4] Several approaches to assimilate HF radar currents have been proposed. *Lewis et al.* [1998] assimilated the surface current estimates for an HF radar system in an ocean model of the Monterrey Bay, California. The observations were incorporated by nudging the surface currents toward the observed currents using a pseudostress. The wind stress was not directly taken into account in this approach. This method appears to be a practical way of ingesting the overall, qualitative characteristics of the current observations, but problems arise if errors in the observations generate unrealistically large divergence and convergence in the model. *Lewis et al.* [1998] proposed to remove the nondivergent signal from the observations before assimilation. In the present paper, we will leave the observations as they are, but we will reduce the gravity waves from the correction introduced by the assimilation [*Barth et al.*, 2007b].

[5] *Breivik and Satra* [2001] assimilated HF radar currents in a high resolution Princeton Ocean Model of the Fedje area of the Norwegian Sea. An ensemble of model states sampled from a reference run was used to prescribe the error covariance of the model. The zonal and meridional velocity components at the intersection of the coverage of both HF radars were used. They showed that the assimilation of the HF radar currents had a positive impact on the model forecasts but that the beneficial impact of the assimilation disappeared after a time-scale of about 6 h.

[6] *Oke et al.* [2002] used an ensemble of 18 different summer model states to assimilate HF radar currents into a shelf circulation model off the Oregon coast. The model and the observations were both time-averaged and the analysis increment distributed over time (TDAP, time-distributed averaging procedure). The authors found that the assimila-

[1] GeoHydrodynamics and Environment Research, MARE, University of Liège, Liège, Belgium.
[2] College of Marine Science, University of South Florida, St. Petersburg, Florida, USA.

0148-0227/08/2007JC004585$09.00

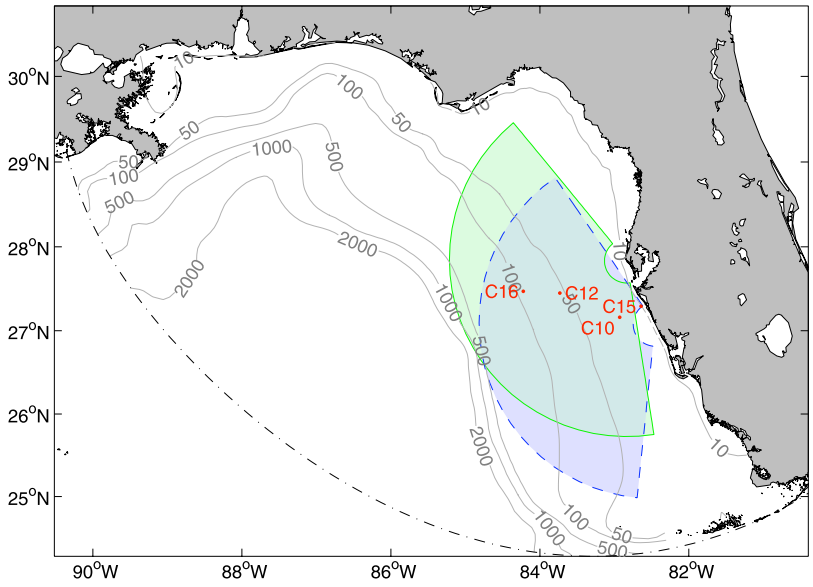

Figure 1. Domain of the WFS ROMS model delimited by the black dash-dotted line and the maximal range of the CODAR antenna at the Redington Shore (solid line) and Venice sites (dashed line). The locations of the ADCP stations C10, C12, C15, and C16 is also shown.

tion compensated for unrepresented components of the applied wind stress and wind stress curl.

[7] A technique based on physical and statistical principles is the approach of *Paduan and Shulman* [2004]. The statistical method Physical-space Statistical Analysis System [*Cohn et al.*, 1998] was used to obtain a surface velocity correction over the model domain, as well as physically based assumptions to project it vertically. In one approach, a wind stress correction was computed such that the work of the wind on the ocean surface is conserved. Another procedure consisted in using the Ekman solution of the wind-driven ocean surface to project the surface velocity increment to depth. Both approaches showed an overall improvement of the model solution relative to unassimilated ADCP current measurements.

[8] An ensemble of model states at different times is often used to prescribe the error covariance. The underlying assumption is that the time variability can be related to the error covariance. However, in most cases, the error covariance is expected to be smaller than the time variability and the time variance needs to be scaled to a realistic level. This is particularly evident for the annual temporal variability of temperature which contains the seasonal cycle, but this procedure generates also long-range spatial correlations due to the fact that the ocean heats or cools in a spatially uniform way. In the present paper, we will estimate the model error covariance by an ensemble of model simulations using different wind-forcings. This avoids the problem of dealing with model states at different times. However, since this approach is computationally intensive, the model ensemble is generated once and kept constant over time, in analogy to an optimal interpolation approximation.

[9] The model simulations are realized for an entire year to test the assimilation scheme under different flow regimes. Tides are removed from the surface current observations and we choose to average the currents over 2 d. This conservative choice was guided by the fact that an assimilation performed too frequently can also degrade the model solution [*Talagrand*, 1972]. Consequently, tides are not included in the model either.

[10] The model used for this study will be presented in section 2. In section 3 the computation of the model error covariance is explained. Section 4 details the assimilation scheme used. The results are presented in section 5 and we summarize our findings in the conclusions (section 6).

2. West Florida Shelf Model

[11] The West Florida Shelf (WFS) model is based on ROMS (Regional Ocean Model System [*Shchepetkin and McWilliams*, 2005]), a hydrostatic, three-dimensional, primitive equation, free-surface model using an s-coordinate in the vertical. The horizontal curvilinear grid resolution varies from 4 km near the coast to 10 km at the open boundary, which matches approximately the resolution of the outer model. The model domain is shown in Figure 1. The vertical grid of the WFS ROMS model contains 32 terrain-following levels. The barotropic and baroclinic model time steps are 6.6 s and 400 s respectively. This model is nested (one-way) into the North Atlantic Hybrid Coordinate Model (NAT HYCOM) run by the Naval Research Laboratory, MS, USA [*Chassignet et al.*, 2007]. The model nesting allows for the inclusion of a realistic Loop Current (LC) in the WFS model. Like the NAT HYCOM, the WFS model surface heat flux is forced by NOGAPS (Navy Operational Global Atmospheric Prediction System) variables, in particular, air temperature, relative humidity, cloud fraction and short-wave radiation. The other heat flux components (latent and sensible heat flux and long-wave radiation) are computed by the WFS model internally using bulk formulae [*Fairall et al.*, 1996]. As wind-forcing the model uses an optimal interpolated (OI) wind field

combining NCEP NAM winds (National Centers for Environmental Prediction, North American Mesoscale Model) with in situ wind measurements [*Alvera-Azcárate et al.*, 2006]. The model currents are in general more accurate with this wind-forcing than the model solution obtained with NOGAPS winds [*He et al.*, 2004; *Barth et al.*, 2008b].

[12] The model surface temperature is relaxed to a cloud-free OI SST based on AVHRR (Advanced Very High Resolution Radiometer), GOES (Geostationary Operational Environmental Satellites), MODIS (MODerate Resolution Imaging Spectroradiometer) and TMI (TRMM Microwave Imager), as described by *He et al.* [2003]. The heat flux correction has the following form [*Barnier et al.*, 1995]:

$$Q_c = \alpha(T(z=0) - T^o) \tag{1}$$

where T^o is the observed SST, $T(z = 0)$ is the model surface temperature and the coefficient $\alpha = -47$ W m^{-2} K^{-1}. The model is also forced by river inflow using the US Geological Survey climatological river runoffs from for the Mississippi, Mobile, Apalachicola, Suwannee, Hillsborough, Caloosahatchee and Shark Rivers.

[13] Finally, the WFS ROMS model implementation uses the Mellor-Yamada 2.5 turbulence scheme [*Mellor and Yamada*, 1982] and the horizontal pressure gradient is computed using the spline density Jacobian formulation by *Shchepetkin and McWilliams* [2003]. More details about the model implementation, in particular of the model nesting, are given by *Barth et al.* [2008a, 2008b].

3. Model Error Covariance and Ensemble Generation

[14] An ensemble of model states reflecting the model error has been generated to provide an ensemble representation of the model error covariance **P**.

$$\mathbf{P} = \frac{1}{N}\mathbf{X}'\mathbf{X}'^T \tag{2}$$

where $\mathbf{X}'$ is a $n \times N$ matrix. The size of the model state vector is n and N is the ensemble size. Each column of this matrix represents an ensemble member minus the ensemble mean. In principle, the ensemble members are generated taking all possible model imperfections (including its forcings) into account. This model error covariance can thus be obtained independently from the assimilated observations. However, in practice only a small subspace of the model error space can be constrained by the observations. Any error mode **x** with no (significant) projection on the space controlled by the observations (i.e., the columns of the observations matrix **H**),

$$\mathbf{Hx} = 0, \tag{3}$$

will not contribute to the model analysis. For efficiency, it therefore makes sense to only include error modes in the ensemble that can be controlled by the observations. For example, the heat fluxes have certainly errors, but it is not expected that the assimilation of HF radar currents can control those errors. The heat fluxes are therefore not perturbed to create the ensemble of model states.

3.1. Ensemble of Wind Fields

[15] The assumption is made that most of the model surface current error on the shelf can be attributed to erroneous wind-forcing. The ensemble of model states are consequently obtained from an ensemble model run with perturbed wind-forcing. All model states produced this way will have different surface currents and therefore each associated error mode will have a significant projection to the vector space controlled by the observations.

[16] An ensemble of 100 wind fields is obtained by perturbing the central OI wind field. The spatial structure of these perturbations is given by EOFs (Empirical Orthogonal Functions). The matrix **W** containing the zonal u^a and meridional v^a wind components, is defined as:

$$\mathbf{W}_{ij} = u^a_{ij} \tag{4}$$

$$\mathbf{W}_{i+m,j} = v^a_{ij} \tag{5}$$

where i is the spatial index ($1 \le i \le m$) and j is the temporal index ($1 \le j \le n$). The size of the matrix **W** is thus $2m \times n$. We used the wind fields over the WFS domain for 2004 at a 6-h frequency. Wind fields anomalies $\mathbf{W}'$ are formed by removing the temporal average. A classical multivariate EOF decomposition is performed with those wind anomalies, limited to the r dominant EOFs (here $r = 60$ based on the eigenvalue spectrum),

$$\mathbf{W}' \sim \mathbf{U\Sigma V}^T \tag{6}$$

[17] The EOFs **U** are used to produce multivariate, spatial perturbations of the wind field:

$$\mathbf{W}^{(k)} = \mathbf{W} + \mathbf{U\Sigma A}^{(k)} \tag{7}$$

where $\mathbf{A}^{(k)}$ is a $r \times n$ matrix containing random time series and where the superscript k represents the ensemble member. All properties of the spatial wind fields that can be expressed by a linear relationship,

$$\mathbf{DW}_j = \mathbf{C}, \text{ for all } 1 \le j \le n \tag{8}$$

where $\mathbf{W}_j$ is the jth column of matrix **W**, and **D** and **C** are matrices of appropriate size, are also respected by the perturbed wind fields:

$$\mathbf{DW}^{(k)}_j = \mathbf{C}, \text{ for all } 1 \le j \le n \tag{9}$$

[18] In particular, the divergence of the perturbed wind field is of the same order of magnitude than the divergence in the unperturbed wind. This desirable property would not have been obtained if both wind fields components were perturbed independently.

[19] The random time series (rows of $\mathbf{A}^{(k)}$) in equation (7) have a standard deviation of $\frac{1}{3}$ and a correlation timescale of $L = 7$ d, meaning that the expected error in the wind field is one third of its variability.

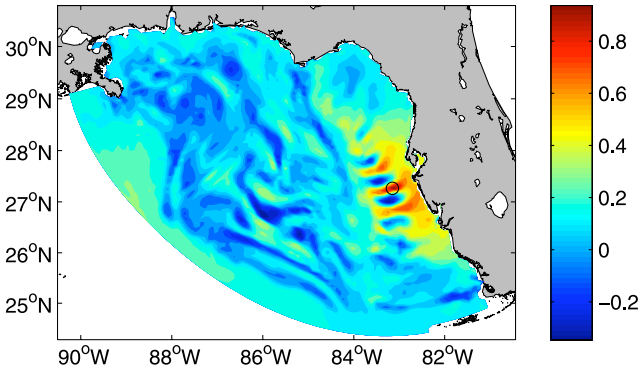

Figure 2. Instantaneous correlation between the *u*-velocity at a specific location marked by the circle and the *u*-velocity at all other model grid points for the ensemble members on 30 January 2004.

3.2. Model Ensemble

[20] The ensemble simulation starts on 1 January 2004 from initial conditions obtained from NAT HYCOM. Each ensemble member uses the same initial conditions but different wind-forcings. In theory, the integration period of the ensemble should be related to the interval between assimilation cycles. Since errors in the initial conditions were not taken into account in this ensemble simulation, each ensemble member was integrated for 30 d in order to develop a realistic large ensemble variance. The ensemble standard deviation of the surface current is about 7.2 cm/s on the WFS.

[21] It is also interesting to study the spatial structure of the covariance. Figure 2 shows the correlation of the zonal velocity at a given point (marked with a circle) and the zonal-velocity at all other surface grid points. The structure of this spatial correlation pattern is surprisingly rich. Near the location of the chosen point, the correlation exhibits sinusoidal variations. The observed AVHRR SST and the modeled SST of the first member of the ensemble are shown in Figure 3. The chosen point for the correlation is located in a temperature front and meandering small-scale structures are visible in the model SST. The position and the presence of these small scale features are qualitatively confirmed by AVHRR SST observations. The instabilities of this temperature front are related to baroclinic instabilities. This front is present in each member of the ensemble simulation, but the phase of the wave-like temperature front is different. This situation results in the particular correlation structure of Figure 2, since the velocity of a chosen grid point is negatively correlated with the velocity at a half-wavelength distance and positively correlated with the velocity at an entire wavelength distance.

[22] This particular correlation pattern can also be derived analytically under idealized conditions. We assume that the *x*-coordinate is parallel to the mean axis of the front. For baroclinic instabilities, the space and time dependent stream function can be written as:

$$\psi = \overline{\psi} + a_\psi e^{i(\omega t - kx + \phi)} \tag{10}$$

[23] As usual, the physical variables correspond to the real part of the complex quantities. $\overline{\psi}$ is the stream function of the background flow balancing geostrophically the density gradient. The exact relationship between frequency ω and wave number k of the meanders is not important for the following derivation. The velocity perpendicular to the front is obtained by:

$$v = -\frac{\partial \psi}{\partial x} = -\frac{\partial \overline{\psi}}{\partial x} + i a_v e^{i(\omega t - kx + \phi)} \tag{11}$$

where a_v is the velocity amplitude of the meander. The frontal system will be in a slightly different state in every ensemble member. The background state ($\overline{\psi}$) will be similar but the phase ψ and to a lesser degree the wave number k will be different from one ensemble member to another. Parameters ψ and k are treated as random variables, and each ensemble member corresponds to a realization of these parameters. In particular, we assume that k follows a Gaussian distribution with mean k' (the true wave number) and variance σ_k^2, and that the phase follows a uniform distribution with values between 0 and 2π. The ensemble mean of the velocity v in such system is the velocity of the background flow,

$$E[v] = -\frac{\partial \overline{\psi}}{\partial x} + i a_v E\left[e^{i(\omega t - kx + \phi)}\right] = -\frac{\partial \overline{\psi}}{\partial x} \tag{12}$$

since one value for the phase ψ and its opposite phase are equally likely. The mesoscale variations are averaged out by the ensemble mean as expected. The deviation around the statically mean state is therefore:

$$v' = v - E[v] = i a_v e^{i(\omega t - kx + \phi)} \tag{13}$$

[24] The spatial covariance between the *v*-velocities at two given positions (x_1 and x_2) at the same time t can be written as:

$$E\left[v(x_1)' v(x_2)'^*\right] = a_v^2 e^{ik'(x_2 - x_1)} e^{-(x_2 - x_1)^2 \sigma_k^2 / 2}, \tag{14}$$

where the star (*) denotes the complex conjugate. This spatial correlation is directly related to the spatial covariance

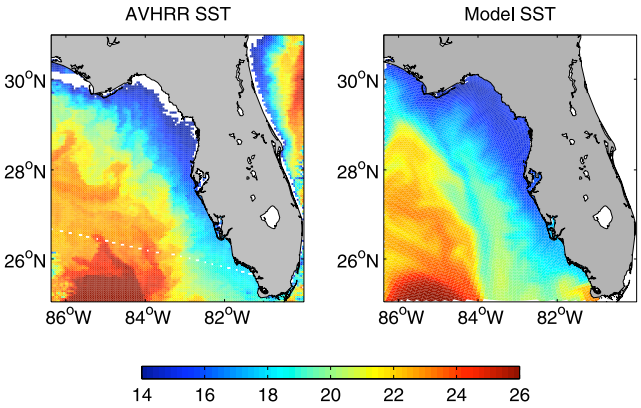

Figure 3. AVHRR SST and model SST on 29 January 2004.

since the variance is a_v^2 everywhere. The correlation between the velocity at x_1 and x_2 can thus be written as,

$$\mathrm{corr}(v(x_1), v(x_2)) = \cos(k'(x_2 - x_1))e^{-(x_2-x_1)^2\sigma_k^2/2} \quad (15)$$

[25] Without an uncertainty in the wave number ($\sigma_k = 0$), the analytical correlation pattern would behave like a cosine. The cosine term in equation (15) is therefore due to the uncertainty in the phase of the meanders in the frontal system. The second term is a Gaussian function depending on the distance between the two points and it stems from an uncertainty in the wave number. A Gaussian correlation function is indeed chosen in several applications of the optimal interpolation scheme and it reflects our intuition that only nearby points are correlated. However, the sinusoidal variations of the correlation are intrinsic to frontal systems. They arise in the ensemble correlation through constructive and destructive interference of the several wave-like current structures associated to the frontal system. This is similar to the interference pattern of light in the classical double-slit experiment of Young, where the covariance behaves like the light intensity (both are indeed quadratic quantities).

4. Data Assimilation

4.1. Analysis Scheme

[26] The data assimilation scheme is based on the Kalman filter analysis. The best linear unbiased estimator (BLUE) of the model's state vector given the model forecast $\mathbf{x}^f$ with error covariance $\mathbf{P}^f$ and the observations $\mathbf{y}^o$ with error covariance $\mathbf{R}$ is given by $\mathbf{x}^a$:

$$\mathbf{x}^a = \mathbf{x}^f + \mathbf{K}\left(\mathbf{y}^o - \mathbf{H}\mathbf{x}^f\right) \quad (16)$$

$$\mathbf{K} = \mathbf{P}^f\mathbf{H}^T\left(\mathbf{H}\mathbf{P}^f\mathbf{H}^T + \mathbf{R}\right)^{-1} \quad (17)$$

$$\mathbf{P}^a = \mathbf{P}^f - \mathbf{K}\mathbf{H}\mathbf{P}^f \quad (18)$$

where $\mathbf{H}$ is the observation operator extracting the observed part of the state vector. If $\mathbf{P}^f$ has a low rank, then the error covariance can be efficiently expressed in form of its square root matrices [*Tippett et al.*, 2003]:

$$\mathbf{P}^f = \mathbf{S}^f\mathbf{S}^{fT} \quad (19)$$

[27] The Kalman gain can then be written as [*Brankart et al.*, 2003]:

$$\mathbf{K} = \mathbf{S}^f\mathbf{U}(\mathbf{I} + \mathbf{\Lambda})^{-1}\mathbf{U}^T\left(\mathbf{H}\mathbf{S}^f\right)^T\mathbf{R}^{-1} \quad (20)$$

where $\mathbf{U}$ and $\mathbf{\Lambda}$ are defined by the following eigenvector-decomposition:

$$\left(\mathbf{H}\mathbf{S}^f\right)^T\mathbf{R}^{-1}\left(\mathbf{H}\mathbf{S}^f\right) = \mathbf{U}\mathbf{\Lambda}\mathbf{U}^T \quad (21)$$

[28] If we insert the Kalman gain (20) in equation (17), we obtain the expression for the a posteriori state:

$$\mathbf{x}^a = \mathbf{x}^f + \mathbf{S}^f\mathbf{U}(\mathbf{I} + \mathbf{\Lambda})^{-1}\mathbf{U}^T\left(\mathbf{H}\mathbf{S}^f\right)^T\mathbf{R}^{-1}\left(\mathbf{y}^o - \mathbf{H}\mathbf{x}^f\right) \quad (22)$$

[29] This equation shows that the correction introduced by the analysis is a linear combination of the columns of $\mathbf{S}^f$. This property is common to all assimilation methods based on a reduced rank error covariance of the model state. This approximation assumes that the model is perfect along the directions not included in the error space defined by the error covariance. It is therefore not surprising that the correction term can only lie inside the space formed by the columns of $\mathbf{S}^f$.

[30] The derivation of the assimilation scheme is mathematically equivalent to the SEEK filter [*Pham*, 2001] and has been used previously in a number of studies [e.g., *Brasseur et al.*, 1999; *Brankart et al.*, 2003; *Testut et al.*, 2003; *Barth et al.*, 2007a; *Vandenbulcke et al.*, 2006].

4.2. Surface Gravity Waves in the Analysis Increment

[31] Surface gravity waves may be produced by the data assimilation if the analysis produces a dynamically unbalanced state. Their dynamics can be described by the linearized shallow water equation model:

$$\frac{\partial\eta}{\partial t} = -\frac{\partial U}{\partial x} - \frac{\partial V}{\partial y} \quad (23)$$

$$\frac{\partial U}{\partial t} = fV - gh\frac{\partial\eta}{\partial x} \quad (24)$$

$$\frac{\partial V}{\partial t} = -fU - gh\frac{\partial\eta}{\partial y} \quad (25)$$

where η is the surface elevation, U and V are the depth-integrated horizontal velocity components, H the water depth and g the acceleration due to gravity. The propagation speed of these waves is $\sqrt{gH}$. For an approximate water depth of 100 m, the speed of the barotropic waves is 31 m/s. This means that barotropic waves cross the footprint of an HF radar antenna (about 200 km) in only 2 h. In this work, we use two-day averaged current fields, and therefore they contain no useful constraint for barotropic waves. Since the assimilated data set does not resolve these fast-moving waves, we implemented a filter to ensure that the assimilation does not introduce barotropic waves in the model.

[32] For a constant depth, the previous equations (23)–(25) can be solved analytically. The general solution is a linear combination of two types of modes: a stationary mode representing the geostrophic equilibrium and a fast moving mode representing inertia-gravity waves. The amplitudes of the later are explicitly set to zero in the assimilation increment. It can be shown that this procedure leads to the following differential equations [*Barth et al.*, 2007b] for the filtered quantities η', U' and V':

$$\left(\frac{\partial^2}{\partial x^2} + \frac{\partial^2}{\partial y^2} - \frac{f^2}{gh}\right)\eta' = \frac{1}{h}\frac{\partial V}{\partial x} - \frac{1}{h}\frac{\partial U}{\partial y} - \frac{f^2}{gh}\eta \quad (26)$$

$$U' = -\frac{gh}{f}\frac{\partial\eta'}{\partial y} \quad (27)$$

$$V' = \frac{gh}{f}\frac{\partial\eta'}{\partial x} \quad (28)$$

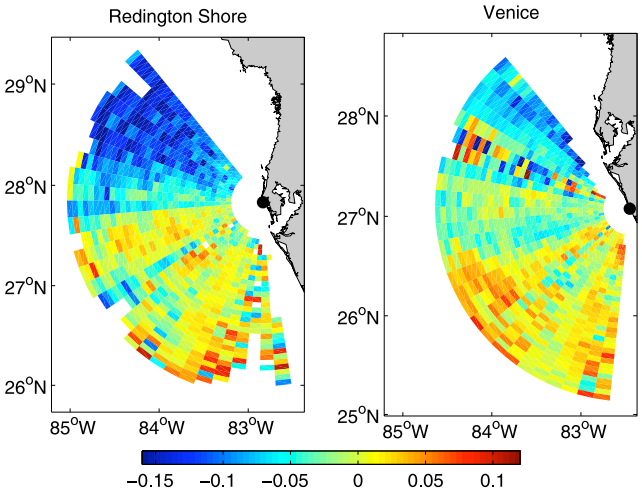

Figure 4. Radial velocities measured from the Redington Shore and Venice sites on 9 December 2005. Positive values represent a current toward the antenna.

[33] This approach conserves potential vorticity, which is used to generalize the previous equation to an arbitrary topography. Numerical tests show that this approach can be used to reduce gravity waves even in the presence of an abrupt shelf break. In the present work, this method is used for the assimilation of observations located on the shelf and we will test its benefit in this context.

[34] The filter is integrated in the assimilation algorithm in the following way.

[35] 1. The analysis increment $\mathbf{x}^i$ is computed according to:

$$\mathbf{x}^i = \mathbf{K}\left(\mathbf{y}^o - \mathbf{H}\mathbf{x}^f\right) \tag{29}$$

[36] 2. The depth-integrated velocity is calculated and the surface elevation is extracted from $\mathbf{x}^i$.

[37] 3. Equations (26)–(28) are solved.

[38] 4. The filtered quantities are replaced in $\mathbf{x}^i$.

[39] 5. The increment $\mathbf{x}^i$ is added to the model forecast $\mathbf{x}^f$ to obtain the analysis $\mathbf{x}^a$.

[40] Since all operations are linear, the filter can be formally written as:

$$\mathbf{x}^a = \mathbf{x}^f + \mathbf{F}\mathbf{K}\left(\mathbf{y}^o - \mathbf{H}\mathbf{x}^f\right) \tag{30}$$

where the filter is expressed as a $n \times n$ matrix $\mathbf{F}$ performing the previous operations on the analysis increment.

4.3. Observations

[41] HF radar sites at Redington Shore and Venice measure the radial velocity components of the ocean surface relative to the HF radar antennas. The CODAR instruments operate at a 26 kHz frequency band centered at 4.55 MHz. The azimuthal resolution is 5° and the radial resolution is 6 km. Radials were generated from the raw spectra data using the SeaSonde processing suite, and were calibrated using measured antenna patterns [*Ullman et al.*, 2006; *Ohlmann et al.*, 2007]. The radials were used at the measured locations and no subsequent spatial interpolation was performed.

[42] The zonal and meridional velocity components can be derived from the radial velocity maps where the range of the antennas intersects. A velocity vector can thus be computed only if the velocity of a water parcel at a given location and at a given time is measured by both antennas. The coverage (in space and time) of the velocity vectors is thus smaller than the coverage of the radial velocity maps. Therefore we choose to assimilate directly the radial currents instead of the total currents. Furthermore, the error between the derived zonal and meridional currents is correlated. This correlation between the observations should be specified in the observations error covariance matrix $\mathbf{R}$. This difficulty does not arise when the original radial currents are used.

[43] Since the model runs do not include tides, the tidal variability has to be subtracted from the HF radar data set. On the basis of all available data from April 2004 to April 2006 at a hourly frequency, tidal parameters of the radial velocity are determined using the T_TIDE package [*Pawlowicz et al.*, 2002]. Only the mayor constituents, i.e., O1, K1, M2, and S2 are included in this analysis. Once these tidal parameters are known, the tidal variation for the four mayor constituents are subtracted from the radial currents. These hourly subtidal currents are then averaged over a two-day time window to reduce the noise inherent to the HF radar currents (see *Barth et al.* [2008a] for more details).

[44] Along with the hourly radial currents, an error map is provided by the HF radar instrument. Since the tidal constituents are computed using a large data set, we assume that the error in the estimated tidal currents is negligible compared to the error in the subtidal currents. The error of the hourly currents is thus used as the error of the subtidal currents. The error variance of the two-day currents is computed as the mean error variance of current maps within the two-day time period.

[45] An example of the radial velocities is shown in Figure 4 for 9 December 2005. Positive radial currents represent a movement toward the CODAR antenna. On this date, the general current is directed northwestward. Despite the two-day averaging period, the radial currents are still quite noisy. The CODAR data therefore presents an interesting and challenging task for data assimilation which aims to optimally reduce the error by combining the model and the data.

4.4. Implementation

[46] The model state vector is composed by the sea level elevation, temperature, salinity and the two horizontal curvilinear velocity components. All those variables are used on the native Arakawa-C model grid.

[47] For each single (scalar) radial HF radar measurement, the model horizontal surface currents components are interpolated bilinearly on the location of the HF radar measurement and then the velocity vector is projected to the radial direction. The velocity perpendicular to the radial direction is thus not directly constrained by the observations but a correction is obtained based on the model error covariance linking all elements of the state vector. Several

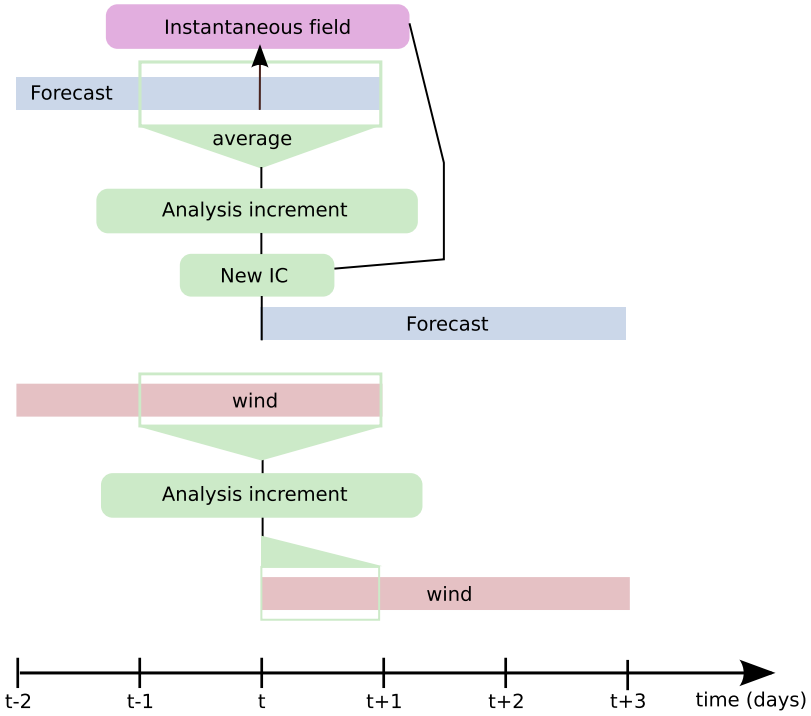

Figure 5. Diagram showing the different sequential steps of the data assimilation algorithm. The computation of the analysis increment is represented as two boxes in the diagram for the displaying purposes, but the analysis increment of the model variables and of the wind stress are performed together in a single step.

assimilation experiments with slightly different setups are conducted.

[48] *AssimRef*: In this experiment the assimilation is performed with 100 member ensemble of instantaneous fields. No postprocessing is applied to the correction.

[49] *AssimAvrEns*: The same as AssimRef, except that the ensemble is composed by 100 members of daily averaged fields.

[50] *AssimFilter*: The same ensemble as AssimRef is used, except that the filter reducing gravity waves is used as a postprocessing step.

[51] *AssimWind*: The state vector at time t now also contains the wind stress components averaged over a two-day interval centered at t, otherwise the experiment is identical to AssimRef. The inclusion of the averaged wind stress vector is a novel aspect of this data assimilation implementation. This allows the data assimilation to correct also the wind stress and therefore the influence of the correction will last after the assimilation.

[52] *AssimAll*: This ensemble is based on daily averaged fields. A gravity wave filter is used and the wind stress is included in the state vector.

[53] The standard sequential assimilation scheme is complicated by the fact that the assimilated currents are two-day averages and cannot be treated as instantaneous and that the two-day averaged wind stress is also part of the state vector in some experiments. Figure 5 shows the adopted assimilation procedure of the experiment AssimAll. Observations (if available) are assimilated every 2 d. The different steps involved in a single assimilation cycle can be listed as follows.

[54] 1. The model is started at $t - 2$ and runs for 3 d.

[55] 2. The forecast model currents are averaged from $t - 1$ to $t + 1$.

[56] 3. The wind stress is also averaged from $t - 1$ to $t + 1$.

[57] 4. The analysis increment is computed based on the model error covariance expressed as an ensemble.

[58] 5. The inertia gravity wave filter is applied to the correction.

[59] 6. This correction is added to the instantaneous model field at t to produce a new initial condition (IC).

[60] 7. The wind stress correction is applied uniformly to the wind-forcing between t and $t + 1$.

[61] For the other assimilation experiments this procedure is accordingly simplified by removing the step 4 or 7 or by using instantaneous fields instead of averaged fields for the ensemble.

[62] The time averaging of the model results computed to match the filtered observations is similar to the approach of *Oke et al.* [2002]. The difference here is that the corrections are not introduced incrementally as it is done in the Time-Distributed Averaging Procedure [*Oke et al.*, 2002] or Incremental Analysis Update [*Bloom et al.*, 1996]. Instead, we implemented the spatial filter [*Barth et al.*, 2007b] and averaged the ensemble fields in an attempt to remove spurious variability before it is introduced into the model.

5. Results

[63] In addition to the data assimilation experiments, a free model run without assimilation was carried out. Re-

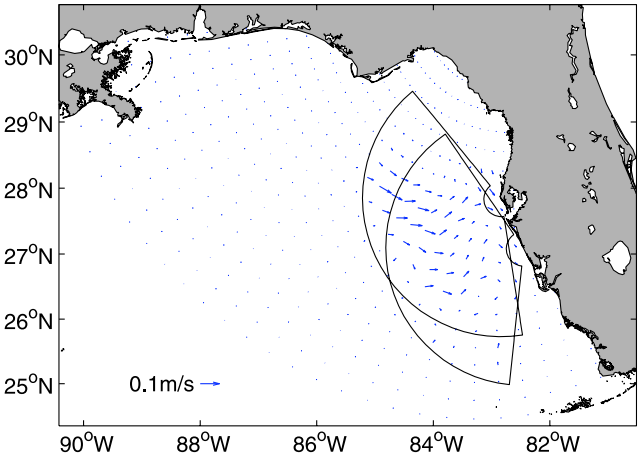

Figure 6. Velocity increments on 9 December 2005.

ferred to as $\mathbf{x}^c$ for control run, this experiment serves as a baseline for assessing the benefit of the assimilation. The mean square error skill score MSESS [*Murphy*, 1988] is used to quantify the improvement over this baseline:

$$\mathrm{MSESS} = 1 - \frac{\mathrm{RMS}(\mathbf{x}^a, \mathbf{y}^o)^2}{\mathrm{RMS}(\mathbf{x}^c, \mathbf{y}^o)^2} \tag{31}$$

where $\mathbf{x}^c$ represents the results from the control run, $\mathbf{y}^o$ represents the observations and $\mathbf{x}^a$ are the results from an assimilation experiment. The model simulations are initialized on 1 January 2005 and run for 1 year. The analysis time step is in general 2 d. At some time-instances, no data are available and therefore no assimilation is performed but this occurred only 7 times. In total, 175 assimilation cycles are performed.

[64] To illustrate the impact of the HF radar assimilation, the velocity correction of the 9 December 2005 (corresponding to the HF radar observation of Figure 4) is shown in Figure 6. From the increments, the effective coverage of the HF radar antennas is visible. In particular, this figure illustrates that a large fraction of the shelf circulation is constrained by the HF radar observation.

5.1. Comparison With HF Radar Currents

[65] In a first test, we compare the model forecast (typically two-day forecasts) with the not yet assimilated observations. The model forecast is not yet influenced by the observations and the forecast is therefore statistically independent from the observations of the same point in time (provided that the time correlation in the observational error can be neglected. We consider a two-day average a sufficiently long time interval for this to be the case). This error measure is useful to assess the benefit of previous assimilation cycles (i.e., how effectively was the information contained in the observations transferred into the model) but also to determine if the assimilation procedure produced a dynamically balanced state, which is particularly important in the assimilation of velocity measurements. Both characteristics are competing requirements since direct insertion of the observations would represent a perfect transfer of the information contained in the observations to the model, but this procedure would result in an unbalanced state and thus lead to a poor model forecast. In the other extreme, the free model run does not suffer from dynamic imbalance (except during the initialization) but the observations are not used at all.

Table 1. Forecast Skill Score Relative to the Free Model Run

Experiment	Skill Score
AssimRef	0.16
AssimAvrEns	0.17
AssimFilter	0.17
AssimWind	0.19
AssimAll	0.21

[66] The RMS error is computed in the observational space, meaning that the ROMS model currents are interpolated to the location of the observations and locally rotated according to the model grid orientation and the direction of the HF radar antenna.

[67] The RMS error of the free model run relative to the HF radar is 8.55 cm/s and the MSESS values in Table 1 are obtained relative to this value. The simulation AssimRef has a skill score of 0.16 which means that its MSE is on average 16% smaller than the free model run.

[68] The skill score is slightly improved by using the average ensemble members instead of the instantaneous fields. Instantaneous states contain some high-frequency variations (notably inertia-gravity waves) which cannot be appropriately constrained by the observations. By averaging the ensemble over 24 h, those variations are filtered out. The small improvement is probably related to the fact that observations are only assimilated every 2 d (or more). Over this time interval, high-frequency variations probably have sufficient time to dissipate. It can be expected that averaging

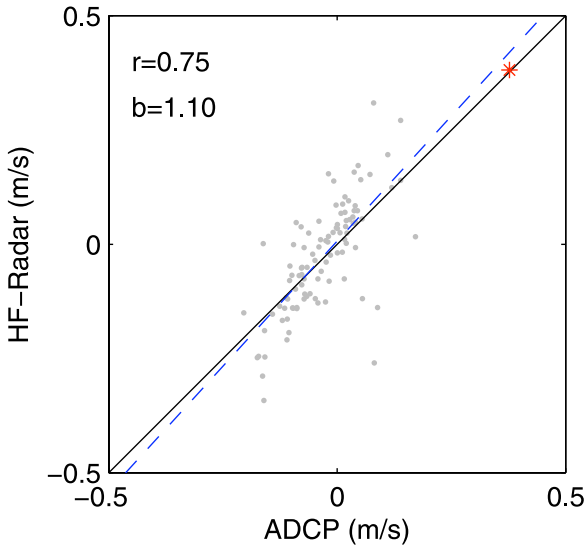

Figure 7. Scatterplot of the top-most ADCP current measurements (4 m depth) at station C10 and HF radar at this station. Both currents are averaged over 2 d. The ADCP currents are rotated to the direction of the HF radar antenna. The velocity generated by Hurricane Dennis is marked with an asterisk. The correlation (r) and regression coefficient (b), which is the slope of the dashed curve, are also shown.

Table 2. MSESS of the Different Assimilation Experiments Relative to the Free Model Run at Different ADCP Stations and the Total Skill Score (Computed by Summation Over Time, Depth and Stations)

Experiment	C10	C12	C15	C16	Total Skill Score
AssimRef	0.21	0.37	0.02	0.28	0.27
AssimAvrEns	0.23	0.36	−0.01	0.32	0.28
AssimFilter	0.24	0.36	0.02	0.31	0.28
AssimWind	0.30	0.37	0.03	0.29	0.29
AssimAll	0.30	0.37	−0.02	0.33	0.30

ensemble members has a larger impact if the observations are assimilated more frequently.

[69] AssimFilter represents also only a small improvement. The purpose of this filter is similar to the averaging of the ensemble members. Its benefit over the approach of AssimAvrEns is the fact that it operates only spatially. In the context of an EnKF [*Evensen*, 2003] with time-varying ensemble, one would need to integrate the ensemble for some time after the assimilation of the observations is carried out to construct centered time averages, a procedure that can significantly increase the CPU time. The spatial filter does not need this since it operates only on instantaneous fields.

[70] The inclusion of the wind field represents the largest single improvement. This is attributed to the fact that most velocity errors in the model are indeed related to errors in the wind-forcing: the benefit of a correct ocean state obtained through data assimilation is rapidly lost if the model continues to be forced by the same (imperfect) wind field. The ocean surface currents adjust to the wind-forcing on a time-scale of $1/f$ according to the Ekman dynamics. This can be considered as the timescale over which the model "forgets" the surface currents initial condition. By correcting the wind-forcing using the covariance between

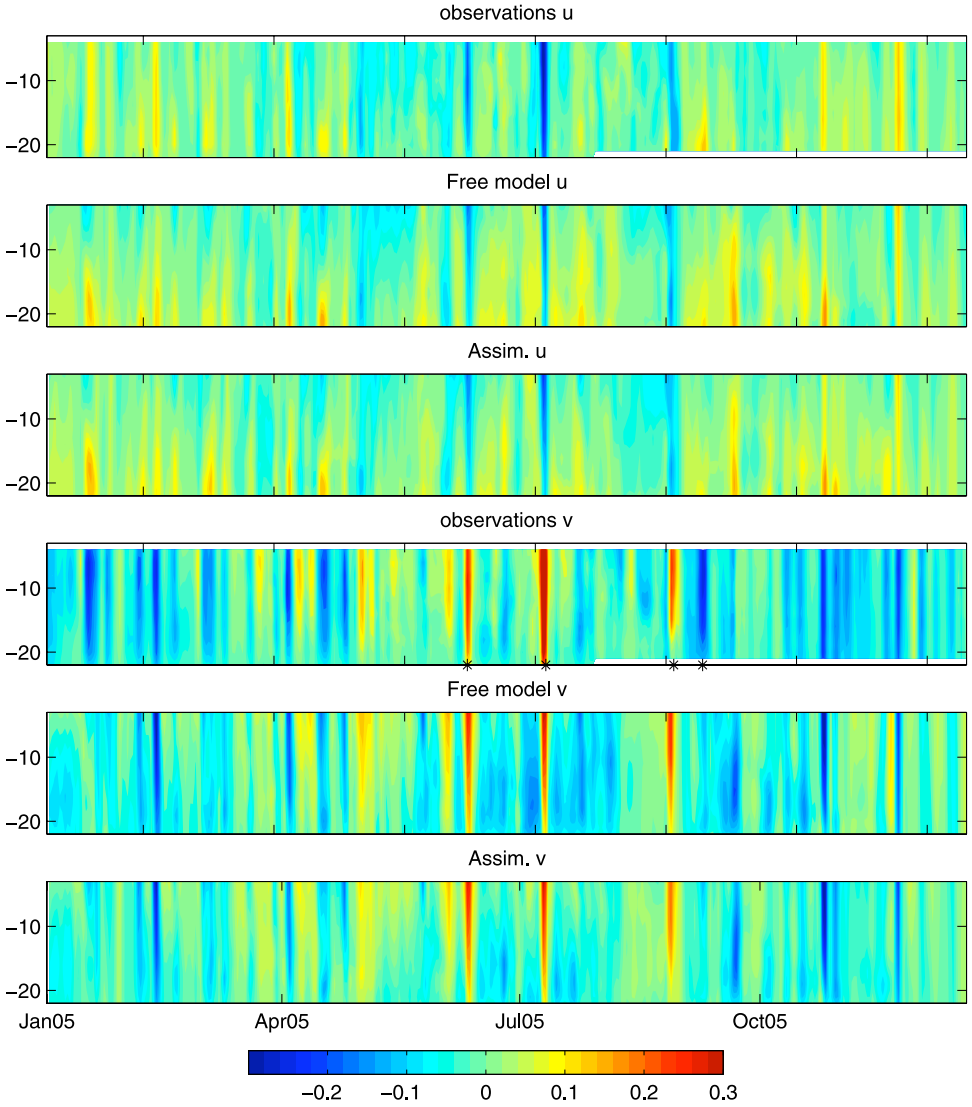

Figure 8. Zonal velocity (u) and meridional velocity (v) at station C10 of the ADCP observations, of the free model run and of the model run with data assimilation as a function of depth (m) and time. Velocities are expressed in m/s. The asterisks on the time axis of the fourth panel represent Tropical Storm Arlene, Hurricane Dennis, Hurricane Katrina and Hurricane Ophelia, in this order.

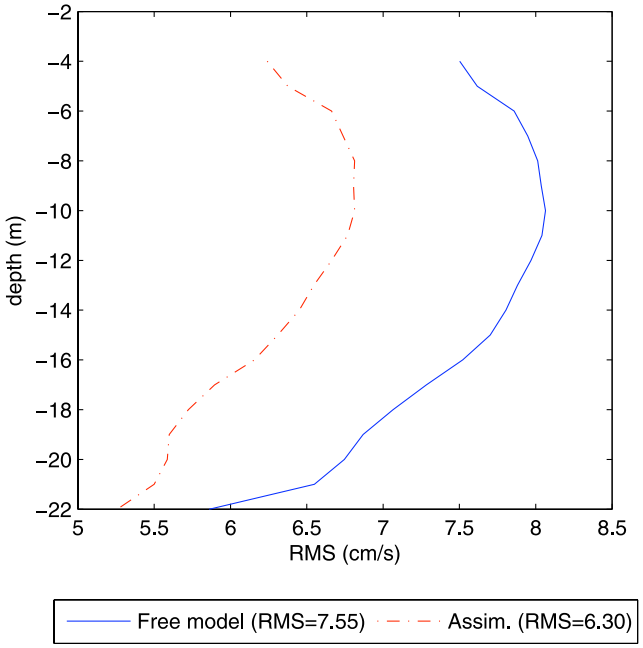

Figure 9. Time-averaged RMS error between ADCP observations at C10 and the model run without assimilation (free model) and with assimilation. The RMS values in the legend represent the depth-averaged RMS error in cm/s.

surface currents and wind stress obtained by the ensemble simulation, the benefit of the assimilation lasts longer.

[71] The experiment AssimAll includes all previous approaches. This simulation is 21% better (in terms of MSE) than the free run and 5% better than the reference assimilation run. This shows that the improvements obtained by the previous tests are not mutually exclusive and that the techniques can be applied together.

5.2. Comparison With Independent ADCP Currents

[72] The previous section compared the model currents to the HF radar currents. Here we will compare the model results with ADCP currents. Several ADCP velocity measurements are available on the WFS at various locations as shown in Figure 1. These observations constitute an independent data set for validating the assimilation procedure in the sense that these data are not used during the model run. The ADCP instruments measure the velocity from the near surface to the near bottom. An error reduction of the surface velocity is to be expected but an improvement of the currents in the remaining water column has yet to be demonstrated.

[73] First, the consistency of the HF radar velocity measurements and the ADCP observations is assessed. Figure 7 shows, as an illustration, the scatterplot of the radial HF radar currents at station C10 from the Redington Shore site and the corresponding surface velocity from station C10 (see Figure 1 for its location). The correlation is in general good and the slope of the regression is not significantly different from 1. The 95% confidence interval of the slope [following *Wilks*, 1995] is [0.91, 1.28] which contains the ideal value of 1. A more extensive comparison has been made by *Kelly et al.* [2003] using the full velocity vector retrieved at the intersection of both antennas, while Figure 7 shows the radial component used in this study. The authors found a correlation of 0.9 for the along-shelf velocity component and 0.62 for the across-shelf velocity component at station C11 (20 m isobath).

[74] Table 2 shows the skill score of the model (by summation over depth and time) for stations C10, C12, C15 and C16 and the total skill score, for the different model experiments. The basic conclusion obtained in section 5.1 is also valid for the ADCP stations: every variant of this assimilation experiment slightly improves the results and the best results are obtained when all are applied together. The improvement of the AssimWind is not as large as previously which is understandable since the wind influences primarily the near surface currents and its impact is smaller when the RMS error is computed over the entire water column.

[75] There is almost no improvement at station C15 (10 m isobath) which lies outside of the domain covered by the HF radar antenna. It should be also noted that the coverage in Figure 1 is the ideal coverage and that the antenna covers most of the time a smaller area (in average 69% of the shown area). The largest improvements are obtained as expected within the range of the HF radar antennas, i.e., at stations C10, C12 and C16.

[76] Surprisingly, the improvement relative to the ADCP currents is larger than the improvement relative to the surface HF radar currents. This can be explained by the fact that the expected error of both instruments is quite different. The purpose of data assimilation is to approach the model simulation to the true ocean state and not to the observations. From the typical error variance of the HF radar and ADCP instruments it is expected that ADCP measurements are closer to the true ocean state than the HF radar velocity measurements.

[77] Next, the temporal and spatial variability of the model and observations are examined for stations C10 and C12. The observed zonal velocity along with the model zonal velocity without and with assimilation (AssimAll) at station C10 is shown in the first three panels of Figure 8. The last three panels of this figure show the corresponding fields of the meridional velocity.

[78] The free model is already in good agreement with the observations at this station. Not only the events with barotropic flow are in good agreement with the observations, the free model is also able to represent to some degree the baroclinic events related to strong currents. The time-averaged RMS error between observations and model results for different depths is computed:

$$\mathrm{RMSE}_k = \left[\frac{1}{N}\sum_{n=1}^{N}\left(u_{n,k}-u^o_{n,k}\right)^2+\left(v_{n,k}-v^o_{n,k}\right)^2\right]^{\frac{1}{2}} \qquad (32)$$

where k is the depth index ($1 \le k \le K$) and n is the time index ($1 \le n \le N$) and the subscript o refers to the observations. It should be noted that different conventions exist to compute the RMS velocity error. Some authors divide by $2N$ instead of N. In that case the RMS error represents the expected average error of the velocity

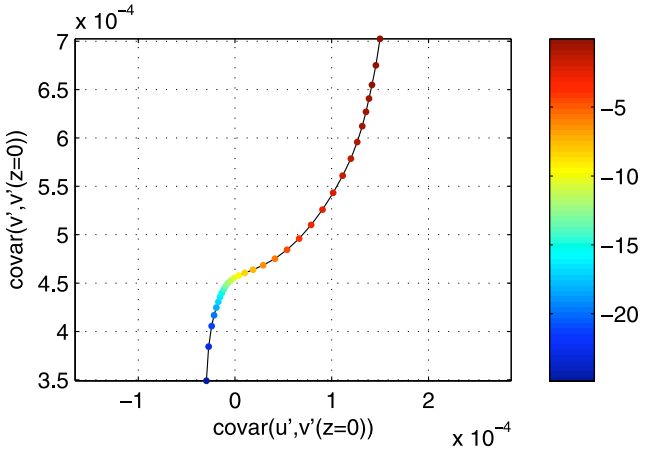

Figure 10. Covariance between the surface along-shelf current component ($v'(z = 0)'$) and the across-shelf (u') and along-shelf (v') current at different depths. The color scale represents the depth (in m).

components. Here we use equation (32) which is the RMS error of the complex quantity $w = u + iv$ [*Kundu*, 1976]. The depth and time averaged RMS errors are computed using:

$$\mathrm{RMSE} = \left[\frac{1}{NK}\sum_{n=1}^{N}\sum_{k=1}^{K}\left(u_{n,k}-u^{o}_{n,k}\right)^2+\left(v_{n,k}-v^{o}_{n,k}\right)^2\right]^{\frac{1}{2}} \quad (33)$$

[79] The RMS errors computed by equations (32) and (33) are shown in Figure 9 for station C10. The error reduction of the model currents is indeed largest at the surface but the error is also reduced over the entire water column. The improvement in relative terms can be quantified using the MSESS, which is 0.33 near the surface and 0.18 near the bottom.

[80] At several occasions from January to May and from September to December, a substantial vertical shear in the u velocity component is observed, coinciding with a strong southward component over a large part of the water column except near the bottom (Figure 8). This current structure

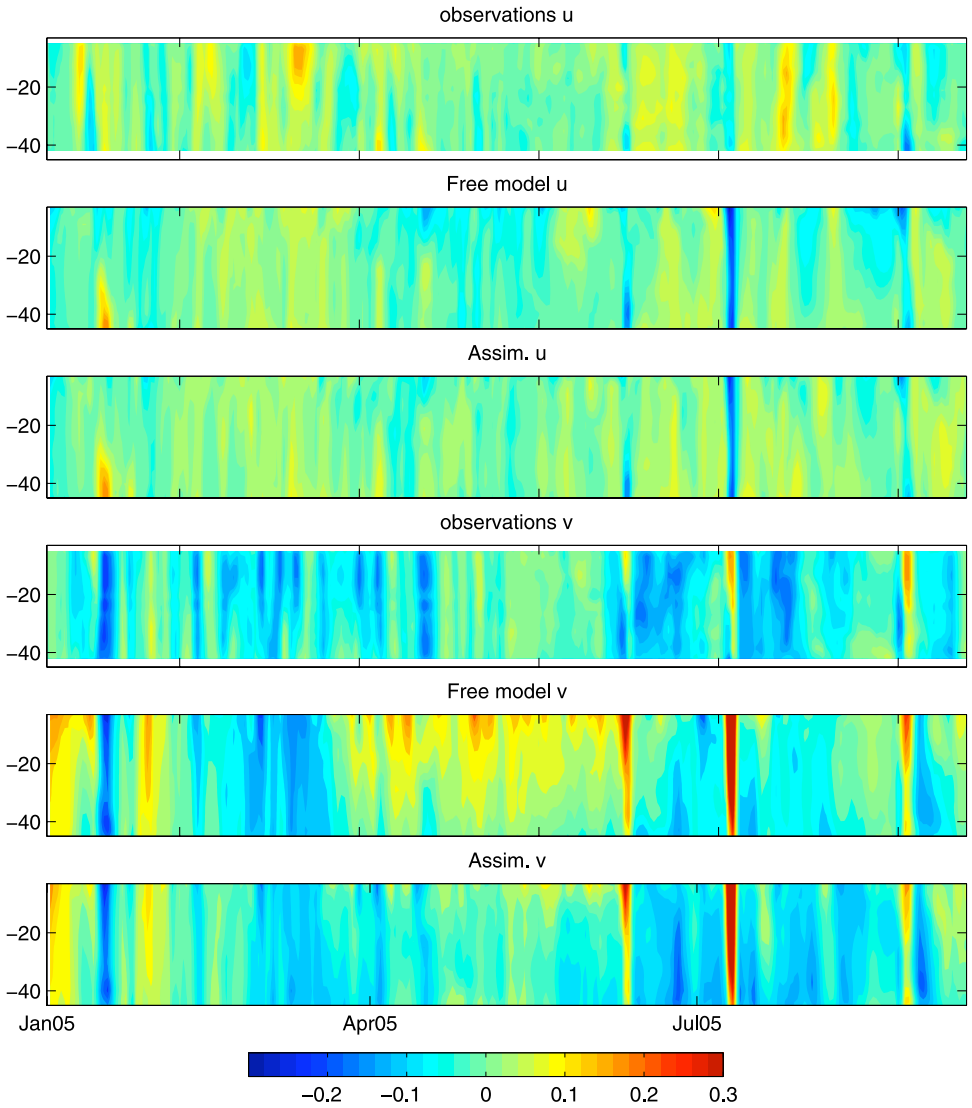

Figure 11. Zonal velocity (u) and meridional velocity (v) at station C12 of the ADCP observations, of the free model run and of the model run with data assimilation as a function of depth (m) and time. Velocities are expressed in m/s.

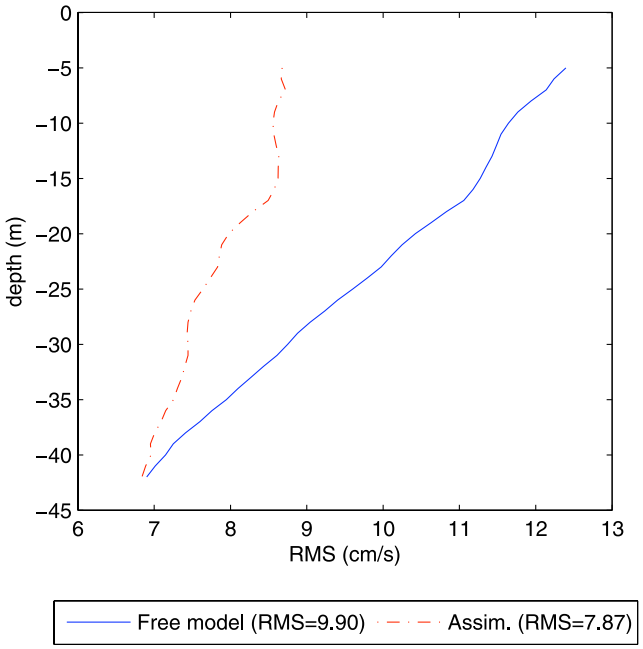

Figure 12. Time-averaged RMS error between ADCP observations at C12 and the model run without assimilation (free model) and with assimilation. The RMS values in the legend represent the depth-averaged RMS error in cm/s.

corresponds to the classical bottom Ekman layer. This feature is in general already well reproduced by the free model simulation which gives us some confidence in the wind-forcing field used (which incorporates in situ winds) and the friction parametrization (surface drag, turbulence closure and bottom drag).

[81] The error covariance is derived from a simulation in January and takes thus the most prevailing situation into account. Figure 10 illustrates the depth dependence of the velocity covariance at station C10 using the ensemble simulation. To facilitate the interpretation, a rotated coordinate system (u', v') is used. The u' component represents the across-shelf velocity (positive means onshore) and the v' component is the along-shelf velocity (positive means a movement to the northwest). Currents on the shelf are predominantly in the along-shelf direction. The covariance between the along-shelf component at the surface ($v'(z = 0)$) and both velocity components at depth is represented in Figure 10. A hypothetical measurement of the along-shelf surface velocity component (with the across-shelf velocity not being measured and thus unconstrained) would yield a correction at depth proportional to the functions given in Figure 10. Over the entire water column, the covariance between the surface along-shelf component and the along-shelf component at depth is positive and decreases. It is indeed expected that an along-shelf measurement produces a correction of the same sign in the along-shelf direction over the entire water column and that the correction decreases with depth. However, the covariance between the surface along-shelf component and the across-shelf component is positive at the surface and becomes negative as depth increases. According to the orientation of the rotated coordinate system, this correlation structure implies that a northwest (southeast) surface current correction would yield an onshore (offshore) current at the surface and an offshore (onshore) current near the bottom. This response of the surface and bottom Ekman layer corresponds to downwelling (upwelling) conditions in agreement with the observed wind-driven circulation on the WFS [*Weisberg et al.*, 2000, 2001; *Liu and Weisberg*, 2005]. The ensemble simulation is thus able to reproduce the dynamical relationship between surface and subsurface currents according to the Ekman balance between friction and Coriolis force.

[82] At station C10, the free model reproduces already quite closely the observations as mentioned earlier. The impact of the assimilation is more visible at station C12, where the model shows an unrealistic northwestward current from April to May (Figure 11). An analysis of the different terms of the momentum equation at these locations reveals that the major forces at this station are the Coriolis force and the vertical friction and that these forces approximately balance themselves according to the Ekman dynamics. The surface current variations are also in phase with the wind variations which indicates that the unrealistic northwestward current is due to errors in the wind field. In the model simulation with data assimilation, the currents during this period are reduced to a more realistic level according to the ADCP observations.

[83] Figure 12 shows the time-averaged RMS errors at station C12. As expected, the RMS error is most significantly reduced at the surface and its impact decreases with depth. Near the bottom (at 40 m depth), the assimilation of the surface currents has almost no impact at this station.

5.3. Tropical Storms and Hurricanes

[84] The 2005 hurricane season was a very active season. The signal of tropical storms and hurricanes is clearly visible in the ADCP measurements. The ADCP record (Figure 8) shows Tropical Storm Arlene (2005-06-11), Hurricane Dennis (2005-07-11), Hurricane Katrina (2005-08-29) and Hurricane Ophelia (2005-09-09). Most storms passed to the west of the WFS and produced a strong northward and northwestward current when closest to the shelf. Hurricane Ophelia, which stayed on the Florida east coast, generated a southward flow on the WFS. Most tropical storms and hurricanes generated a flow over the entire water column at the shelf stations C10 and C12. In some circumstances, bottom friction weakens the flow at depth. The timing of these events is in general well reproduced by the model. The bottom Ekman layer current structure described in the previous section is not observed during extreme events such as Hurricanes Dennis and Katrina. The high turbulent viscosity created by these hurricanes inhibits a vertical shear. The current is uniform over the whole the water column and it is subjected to the resultant force of the surface and bottom drag.

[85] The currents on the shelf generated by Hurricane Dennis are quite uniform horizontally. The spatial dependency of the radial current pattern is induced by the bearing of the antenna. Station C10 is well located and oriented relative to the HF radar antenna to confirm the HF radar measurements. At this location, the HF radar measures a radial current of 0.381 m/s. This value is in good agreement

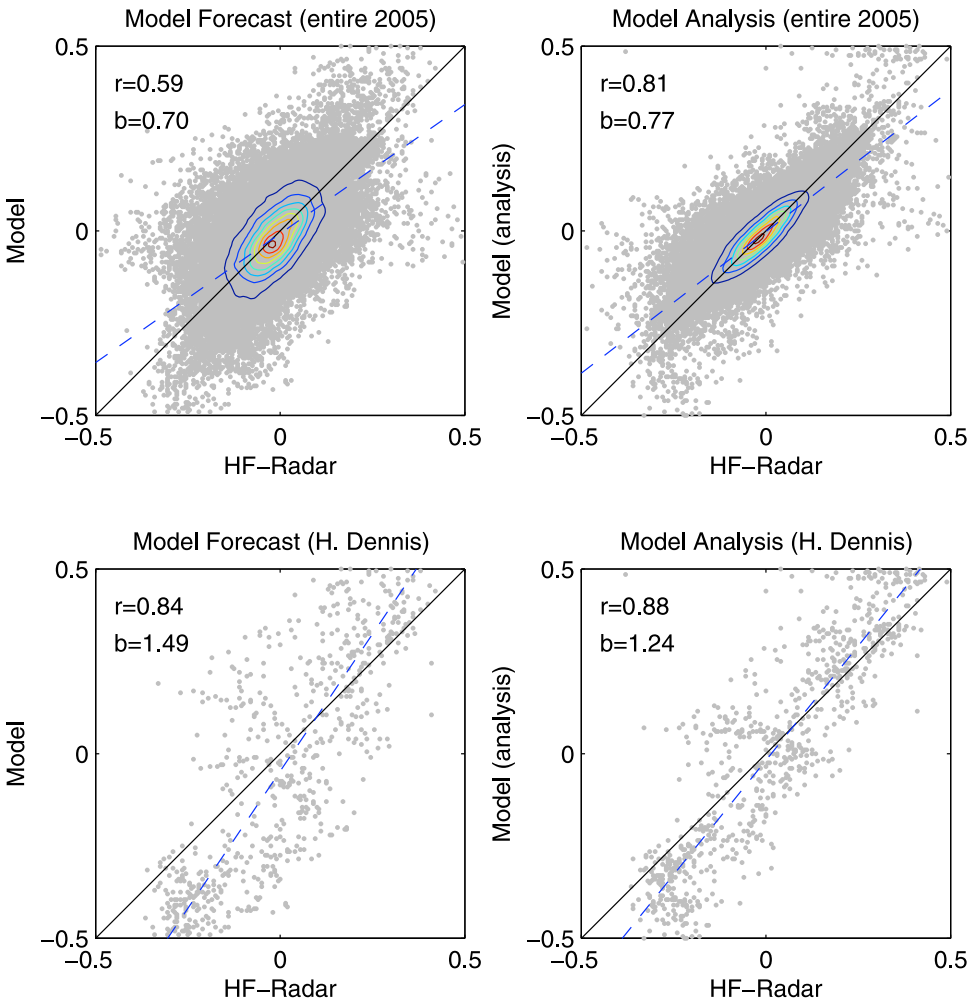

Figure 13. Scatterplots of the model surface currents and HF radar (experiment AssimAll) currents for the Redington Shore site. Model velocities are interpolated to the radial velocities positions and then rotated. The correlation (r) and regression coefficient (b), which is the slope of the dashed curve, are also shown. The contours show the density of the points of the scatterplot. Units are m/s.

with the currents obtained at station C10 rotated toward the antenna, namely 0.377 m/s at the surface bin (Figure 7).

[86] A scatterplot of the radial currents of the Redington Shore site for the entire year 2005 and for Hurricane Dennis is shown in Figure 13. The regression coefficient of the model forecast is 0.7 which indicates that, in average for 2005, the model currents are smaller than the HF radar observations. As expected, the analysis increases the correlation between model and observations, improves the regression coefficient and reduces the spread around the ideal 45° line. Interestingly, the model forecast correlates better with the HF radar observations during Hurricane Dennis. This can be attributed to the fact that events which are so strongly externally forced are easier to predict as long as the forcing is sufficiently accurate. The wavefield is also more energetic so the backscattering signal at the HF radar antenna is higher. However, the model overestimates the currents generated by Hurricane Dennis. The effect of waves induced by the Hurricane can indeed explain a reduction of the drag coefficient [*Kara et al.*, 2007] during high wind regimes. The assimilation of HF radar currents compensates to some extent the missing wave effects but an improved parametrization for strong wind regimes would have most likely a beneficial impact under these circumstances.

6. Conclusions

[87] The present work describes an assimilation system for HF radar currents in a nested West Florida Shelf (WFS) model. The model error covariance is estimated using an ensemble simulation with different wind-forcings. The resulting ensemble contains rich small-scale structures near fronts which can be described as a superposition of ensemble members with different phase, creating a pattern similar to wave interference.

[88] Different variants of the implemented assimilation scheme have been tested using a time-average ensemble, a filter to reduce surface-gravity waves and an extended state vector including wind stress. Each of the techniques improves the two-day model forecast compared to not yet assimilated surface current measurements. The best model simulation is obtained when all of the variants are used

together showing that the obtained benefit is not mutually exclusive.

[89] HF radar currents is a promising data set to constrain the circulation of coastal models providing significant coverage over the WFS model domain. HF radar currents estimates correlate well with more traditional ADCP measurements, even during extreme events such as hurricanes.

[90] The motivation of using the spatial filter to remove spurious barotropic waves from the assimilation increment is similar to the idea of *Lewis et al.* [1998] to remove the divergence from the HF radar observations. We preferred however to filter the assimilation increment which is essentially the model-observation misfit smoothed by the model error covariances since estimating spatial derivatives from noisy observations is in general a delicate task. To remove the divergence it would be also necessary to assimilate total currents. However, if total fields would be used in the present study, the amount available observations would be substantially reduced (since total fields can only be derived at the intersection of the coverage of the two antennas and both antennas have to be operational at the same time).

[91] The vertical error structure was assessed by comparing the model results with independent ADCP measurements. As expected, the largest improvement was observed at the surface but the model skill relative to the free model run was significantly improved also at depth. The currents on the shelf are mostly governed by Ekman dynamics. The vertical structure of the ensemble error covariance reflects this characteristic and to an along-shelf correction at the surface corresponds indeed an across-shelf correction at depth.

[92] Several research directions for improving the assimilation system are possible. In particular, future studies will assess the benefit of a time-varying ensemble using the fully model dynamics. In this case, the error covariance will be adapted to different circumstances and flow regimes (e.g., strong or weak stratification). Also, the combination of HF radar data with other observations needs further research.

[93] **Acknowledgments.** This work was supported by the "Global Ocean Prediction with the Hybrid Coordinate Ocean Model (HYCOM)" program and the "HYCOM Coastal Ocean Hindcasts and Predictions: Impact of Nesting in HYCOM GODAE Assimilative Hindcasts" program of the US Office of Naval Research (grant: N00014-04-1-0676 and N00014-99-1-1051 respectively), plus the Southeast Atlantic Coastal Ocean Observing System, also supported by the US Office of Naval Research (grant: N00014-02-01-0972). In situ data are attributed to the Ocean Circulation Group. Particular thanks go to Rick Cole, Jeff Donovan, Jay Law, Dennis Mayer, Cliff Merz, Jyotika Virmani and Vembu Subramanian. We also thank Sage Lichtenwalner for his help with the CODAR data. The F.R.S.-FNRS, Belgium is acknowledged for the funding of the current postdoctoral positions of A. Barth and A. Alvera-Azcárate. The two anonymous reviewers are acknowledged for their constructive and helpful criticism.

References

Alvera-Azcárate, A., A. Barth, R. W. Helber, R. He, and R. H. Weisberg (2006), Mapped fields of surface geostrophic currents based on altimetry, and fields of sea surface winds, cloud-free sea surface temperature and chlorophyll concentration using monovariate OI and a multivariate EOF technique, *Eos Trans. AGU*, *87*(36), Ocean Sci. Meet. Suppl., Abstract OS15C-06.

Barnier, B., L. Siefridt, and P. Marchesiello (1995), Thermal forcing for global ocean circulation model using a 3-year climatology of ECMWF analyses, *J. Mar. Syst.*, *6*, 363–380.

Barrick, D. (1978), HF radio oceanography–A review, *Boundary Layer Meteorol.*, *13*, 23–43.

Barrick, D., M. Evans, and B. Weber (1977), Ocean surface currents mapped by radar, *Science*, *198*, 138–144.

Barth, A., A. Alvera-Azcárate, J.-M. Beckers, M. Rixen, and L. Vandenbulcke (2007a), Multigrid state vector for data assimilation in a two-way nested model of the Ligurian Sea, *J. Mar. Syst.*, *65*(1–4), 41–59.

Barth, A., J.-M. Beckers, A. Alvera-Azcárate, and R. H. Weisberg (2007b), Filtering inertia-gravity waves from the initial conditions of the linear shallow water equations, *Ocean Model.*, *19*, 204–218.

Barth, A., A. Alvera-Azcárate, and R. H. Weisberg (2008a), Benefit of nesting a regional model into a large-scale ocean model instead of climatology: Application to the West Florida Shelf, *Cont. Shelf Res.*, *28*, 561–573.

Barth, A., A. Alvera-Azcárate, and R. H. Weisberg (2008b), A nested model study of the loop current generated variability and its impact on the West Florida Shelf, *J. Geophys. Res.*, *113*, C05009, doi:10.1029/2007JC004492.

Bloom, S. C., L. L. Takacs, A. M. D. Silva, and D. Ledvina (1996), Data assimilation using incremental analysis updates, *Mon. Weather Rev.*, *124*, 1256–1271.

Brankart, J. M., C.-E. Testut, P. Brasseur, and J. Verron (2003), Implementation of a multivariate data assimilation scheme for isopycnic coordinate ocean models: Application to a 1993–96 hindcast of the North Atlantic Ocean circulation, *J. Geophys. Res.*, *108*(C3), 3074, doi:10.1029/2001JC001198.

Brasseur, P., J. Ballabrera, and J. Verron (1999), Assimilation of altimetric data in the mid-latitude oceans using the Singular Evolutive Extended Kalman filter with an eddy-resolving, primitive equation model, *J. Mar. Syst.*, *22*(4), 269–294.

Breivik, O., and O. Satra (2001), Real time assimilation of HF radar currents into a coastal ocean model, *J. Mar. Syst.*, *3–4*, 161–182.

Chassignet, E. P., H. E. Hurlburt, O. M. Smedstad, G. R. Halliwell, P. J. Hogan, A. J. Wallcraft, R. Baraille, and R. Bleck (2007), The HYCOM (HYbrid Coordinate Ocean Model) data assimilative system, *J. Mar. Syst.*, *65*, 60–83.

Cohn, S. E., A. da Silva, J. Guo, M. Sienkiewicz, and D. Lamich (1998), Assessing the effects of data selection with the DAO Physical-space Statistical Analysis System, *Mon. Weather Rev.*, *126*(11), 2913–2926.

Evensen, G. (2003), The Ensemble Kalman Filter: Theoretical formulation and practical implementation, *Ocean Dyn.*, *53*, 343–367.

Fairall, C., E. Bradley, D. Rogers, J. Edson, and G. Young (1996), Bulk parameterization of air-sea fluxes for TOGA COARE, *J. Geophys. Res.*, *101*, 3747–3764.

He, R., R. H. Weisberg, H. Zhang, F. Muller-Karger, and R. W. Helber (2003), A cloud-free, satellite-derived, sea surface temperature analysis for the West Florida Shelf, *Geophys. Res. Lett.*, *30*(15), 1811, doi:10.1029/2003GL017673.

He, R., Y. Liu, and R. H. Weisberg (2004), Coastal ocean wind fields gauged against the performance of an ocean circulation model, *Geophys. Res. Lett.*, *31*, L14303, doi:10.1029/2003GL019261.

Kara, A. B., E. J. Metzger, and M. A. Bourassa (2007), Ocean current and wave effects on wind stress drag coefficient over the global ocean, *Geophys. Res. Lett.*, *34*, L01604, doi:10.1029/2006GL027849.

Kelly, F. J., J. S. Bonner, J. C. Perez, D. Trujillo, R. H. Weisberg, M. E. Luther, and R. He (2003), A comparison of near-surface current measurements by ADCP and HF Radar on the West Florida Shelf, in *Proceedings of the IEEE/OES Seventh Working Conference on Current Measurement Technology*, pp. 70–74, San Diego, Calif., doi:10.1109/CCM.2003.1194286.

Kundu, P. K. (1976), Ekman veering observed near the ocean bottom, *J. Phys. Oceanogr.*, *6*, 238–242.

Lewis, J. K., I. Shulman, and A. F. Blumberg (1998), Assimilation of CODAR observations into ocean models, *Cont. Shelf Res.*, *18*, 541–559.

Liu, Y., and R. H. Weisberg (2005), Patterns of ocean current variability on the West Florida Shelf using the self-organizing map, *J. Geophys. Res.*, *110*, C06003, doi:10.1029/2004JC002786.

Mellor, G., and T. Yamada (1982), Development of a turbulence closure model for geophysical fluid problems, *Rev. Geophys.*, *20*(4), 851–875.

Murphy, A. H. (1988), Skill scores based on the mean square error and their relationships to the correlation coefficient, *Mon. Weather Rev.*, *116*, 2417–2424.

Ohlmann, C., P. White, L. Washburn, E. Terrill, B. Emery, and M. Otero (2007), Interpretation of coastal HF radar-derived surface currents with high-resolution drifter data, *J. Atmos. Oceanic Technol.*, *24*, 666–680, doi:10.1175/JTECH1998.1.

Oke, P. R., J. S. Allen, R. N. Miller, G. D. Egbert, and P. M. Kosro (2002), Assimilation of surface velocity data into a primitive equation coastal ocean model, *J. Geophys. Res.*, *107*(C9), 3122, doi:10.1029/2000JC000511.

Paduan, J. D., and I. Shulman (2004), HF radar data assimilation in the Monterey Bay area, *J. Geophys. Res.*, *109*, C07S09, doi:10.1029/2003JC001949.

Pawlowicz, R., B. Beardsley, and S. Lentz (2002), Classical tidal harmonic analysis including error estimates in MATLAB using T_TIDE, *Comput. Geosci.*, *28*, 929–937.

Pham, D. T. (2001), Stochastic methods for sequential data assimilation in strongly nonlinear systems, *Mon. Weather Rev.*, *129*, 1194–1207.

Shchepetkin, A., and J. McWilliams (2003), A method for computing horizontal pressure-gradient force in an oceanic model with a non-aligned vertical coordinate, *J. Geophys. Res.*, *108*(C3), 3090, doi:10.1029/2001JC001047.

Shchepetkin, A., and J. McWilliams (2005), The Regional Oceanic Modeling System: A split-explicit, free-surface, topography-following-coordinate ocean model, *Ocean Modell.*, *9*, 347–404.

Talagrand, O. (1972), On the damping of high-frequency motions in four-dimensional assimilation of meteorological data, *J. Atmos. Sci.*, 1547–1571.

Testut, C.-E., P. Brasseur, J.-M. Brankart, and J. Verron (2003), Assimilation of sea-surface temperature and altimetric observations during 1992–1993 into an eddy permitting primitive equation model of the North Atlantic Ocean, *J. Mar. Syst.*, *40–41*, 291–316.

Tippett, M. K., J. L. Anderson, C. H. Bishop, T. M. Hamill, and J. S. Whitaker (2003), Ensemble square-root filters, *Mon. Weather Rev.*, *131*, 1485–1490.

Ullman, D. S., J. O'Donnell, J. Kohut, T. Fake, and A. Allen (2006), Trajectory prediction using HF radar surface currents: Monte Carlo simulations of prediction uncertainties, *J. Geophys. Res.*, *111*, C12005, doi:10.1029/2006JC003715.

Vandenbulcke, L., A. Barth, M. Rixen, A. Alvera-Azcárate, Z. B. Bouallegue, and J. Beckers (2006), Study of the combined effects of data assimilation and grid nesting in ocean models: Application to the Gulf of Lions, *Ocean Sci.*, *2*(2), 213–222.

Volkov, D. L., G. Larnicol, and J. Dorandeu (2007), Improving the quality of satellite altimetry data over continental shelves, *J. Geophys. Res.*, *112*, C06020, doi:10.1029/2006JC003765.

Weisberg, R. H., B. D. Black, and Z. Li (2000), An upwelling case study on Florida's west coast, *J. Geophys. Res.*, *105*(C5), 11,459–11,469.

Weisberg, R. H., L. Zhenjiang, and F. Muller-Karger (2001), West Florida shelf response to local wind forcing: April 1998, *J. Geophys. Res.*, *106*(C12), 31,239–31,262.

Wilks, D. S. (1995), *Statistical Methods in the Atmospheric Sciences*, 467 pp., Elsevier, New York.

A. Alvera-Azcárate and A. Barth, GeoHydrodynamics and Environment Research, MARE, AGO, Institut de Physique B5, University of Liège, Allée du 6-Août, 17 4000 Liège, Belgium. (a.barth@ulg.ac.be)

R. H. Weisberg, College of Marine Science, University of South Florida, 140 7th Avenue South, St. Petersburg, FL 33701, USA.